JOURNAL OF SPACECRAFT AND ROCKETS
Vol. 43, No. 4, July–August 2006

Study of the Ignition Overpressure Suppression Technique by Water Addition

Francisco Canabal*
NASA Marshall Space Flight Center, Huntsville, Alabama 35812
and
Abdelkader Frendi†
University of Alabama in Huntsville, Huntsville, Alabama 35899

The main objective of this study is to gain an understanding of the mechanisms responsible for the suppression of the ignition overpressure observed when water is injected through discrete nozzles into a rocket exhaust. A simplified launch-vehicle/launchpad configuration of relevant importance is selected for this study. This configuration is then numerically modeled using two-phase computational fluid dynamics with a representative motor startup sequence and a series of water addition configurations. The study focuses on the interaction between the ignition overpressure wave and the injected water. Chemical reactions are not included in the model; therefore, the effect of afterburning of fuel-rich exhaust is omitted in this study. A total of 11 water addition configurations were studied. The study demonstrated that ignition overpressure is strongly affected by the cooling of the plume and the amount of obstruction restricting the expansion of the plume. Also, the study suggests the existence of an optimal water addition rate with a weak dependence on the water nozzle pressure drop.

Nomenclature

$\boldsymbol{a}_i^l$	=	convective Jacobian
C	=	water heat capacity
C_d	=	drag coefficient
c_p	=	specific heat at constant pressure
c_v	=	specific heat at constant volume
d	=	droplet diameter; silo diameter
$\boldsymbol{D}$	=	droplet drag vector
D_m	=	droplet drag vector components
E	=	total energy per unit mass
$\boldsymbol{F}_m$	=	inviscid flux vector
$\boldsymbol{g}$	=	Earth gravitational acceleration vector
h	=	convective heat transfer; average element size
h_{fg}	=	heat of evaporation
$(h_g)_i$	=	gaseous enthalpy of species i
k_∞	=	gaseous mixture thermal conductivity at the droplet neighborhood
M	=	Mach number
$\dot{m}$	=	water mass flow rate
$\dot{m}_i'''$	=	mass flow rate of species i per unit volume
Nu_d	=	Nusselt number
P	=	static pressure
p_c	=	combustion chamber total pressure
$\dot{q}$	=	droplet heating rate
R	=	gas constant
$\boldsymbol{R}$	=	residual of the temporal discretization
$\boldsymbol{r}$	=	droplet position vector
r_{32}	=	Sauter mean diameter
Re_d	=	Reynolds number
s, s_1, s_2	=	flow-dependent variation parameters $(0 \le s, s_1, s_2 \le 1)$
T	=	static temperature
T_c	=	combustion chamber total temperature
T_d	=	water droplet temperature
t	=	time
$\boldsymbol{U}$	=	independent variable vector
$\boldsymbol{V}$	=	gaseous mixture velocity vector
$\boldsymbol{V}_d$	=	droplet velocity vector
$(V_m)_i$	=	species i velocity components
$\boldsymbol{V}_\infty$	=	average gaseous mixture velocity vector at the droplet neighborhood
v_m	=	gaseous mixture velocity components
We	=	Weber number
x_m	=	coordinate components
Y_i	=	mass fraction of species i
y	=	droplet deformation
Γ	=	domain surface
Γ_m	=	components of the surface vector
$\Delta \boldsymbol{F}_m$	=	variation in the inviscid flux vector
Δt	=	time step
$\Delta \boldsymbol{U}$	=	variation in the independent variable vector
δ_{ij}	=	Kronecker delta
λ	=	eigenvalues
μ	=	water absolute viscosity
ρ	=	gaseous mixture density
ρ_d	=	water droplet density
ρ_∞	=	average gaseous mixture density at the droplet neighborhood
σ	=	surface tension at the water-gas mixture interface
$\boldsymbol{\Phi}_\alpha$	=	shape function
Ψ	=	limiter function
Ω	=	droplet volume, region of $\mathbb{R}^3$

Subscripts

m, n	=	indices (1, 2, 3)
ss	=	steady-state condition
α	=	global node number
∞	=	far-field conditions

Superscripts

l	=	conditions evaluated at time t
$+$	=	associated with the positive eigenvalues
$-$	=	associated with the negative eigenvalues

Received 30 November 2004; accepted for publication 24 September 2005.

*Aerospace Engineer. Member AIAA.
†Professor, Mechanical and Aerospace Department. Senior Member AIAA.

I. Introduction

DURING the rocket ignition of launch vehicles, a shock wave that travels through the nozzle toward the launchpad, where it is reflected back toward the vehicle is generated. This initial wave is referred to as the ignition overpressure wave. Depending on the maximum overpressure, this wave can induce large vibrations causing damage to the vehicle structure and, although less likely because of the low frequency, damage to the payloads. Therefore, it is important to understand the mechanisms that generate the shock wave and its subsequent propagation over the vehicle. Determination of the maximum overpressure is necessary to protect the content of the payload area and the launch-vehicle's structure.

There exist many ways of generating shock waves in a gas mixture: heat addition, mass addition, and momentum addition. When heat is added to a volume of gas, the density of the gas is reduced; this in turn causes an expansion of the volume occupied by the heated gas, which results in a blast wave. Taylor[1] studied the propagation and decay of blast waves generated by the detonation of an explosive. He defined a blast wave as a sharp wave front followed by an expansion wave. This sharp wave front is also known as the blast-wave overpressure. He found that the spatial decay of the maximum overpressure was inversely proportional to the distance from the source. Sakurai[2] later studied the propagation and decay of spherical blast waves. He used a power series expansion approach to solve the hydrodynamic equations. He found that the decay of the blast waves was inversely proportional to the cubic power of the distance from the source. The maximum overpressure generated by Sakurai's blast waves was much higher than that studied by Taylor. Frendi[3] studied the blast waves generated by a spark ignition device in a chemically reacting gas mixture. He found that the maximum overpressure increases when the energy released by the spark is increased or when the ignition time is decreased.

During the startup process of the rocket motors of underground missiles, such as the Titan or Minuteman, strong pressure waves are generated.[4–6] For silos, the ignition overpressure is further aggravated by the exhaust plume expansion into a confined volume. However, the Titan III, which launches from an open-air launchpad, also experienced a considerable overpressure environment.[7] Likewise, the first space shuttle flight (STS-1, in April 1981) experienced higher than predicted values of structural vibration as a result of the ignition overpressure. Therefore, it became apparent to NASA engineers that the problem of ignition overpressure needed immediate attention. Several experimental studies were initiated to find a solution to this problem. Dougherty et al.[8] studied the effects of adding water to the solid rocket motor exhaust plume. This was found to be effective in reducing the overpressure and was subsequently used in STS-2.

Shapiro and Hawthorne[9] developed a model for water injection into a high-speed gas stream by considering the gaseous and droplet phases as two separate flowing systems so that the conservation equations can be applied separately to each system. These two systems were then coupled through equations that describe the mass, momentum, and heat transfer between flowing systems. Woo et al.[10] used Shapiro's model to study the water-injection problem in a subsonic gas stream. They found that the main effect of the water addition was to increase the density of the exhaust gas stream. Jones[11] studied the scaling of the ignition startup pressure transients in rocket systems as applied to the shuttle overpressure phenomenon. Lai and Laspesa[12] studied the correlation between the overpressure measured on STS-1 and that measured with subscale model tests. They found that the overpressure scales with the square of the chamber pressure rate of increase. The 6.4% scale model they used reproduced the overpressure measured on STS-1. However, the suppression system developed for STS-2 was more effective than the prediction based on the scale model.

Even though water addition has been effectively used to reduce the overpressure, the physics involved in the interaction between the motor plume and the water droplets has not been fully understood. In particular, it is desirable to determine the optimal amount of water needed to achieve a given overpressure reduction and also to determine where, when, and how the water should be injected into the plume to effectively reduce the ignition overpressure.

A simplified model for the water addition was first developed to perform a preliminary analysis. The results from this preliminary analysis facilitated the selection of the water addition configurations to be studied using a higher-fidelity model. Including the configurations in the preliminary analysis, a total of 11 water addition configurations were studied.

II. Mathematical Model

During a launch-vehicle takeoff, the pressure in the motor combustion chamber undergoes a rapid increase until the main stage or steady-state chamber pressure is achieved. This rapid increase in chamber pressure induces a shock wave that propagates away from the motor while interacting with the vehicle and its surroundings. After this initial stage, the chamber pressure assumes its steady-state value, the chamber exhaust flow is choked, and the nozzle plume flowfield reaches its steady-state distribution. Any mathematical model of this phenomenon should describe the generation and propagation of the ignition overpressure and its interaction with a water source.

The approach adopted in this investigation is to have two separate yet coupled models: one governing the nonreacting gaseous flowfield and the other governing the dynamics of the supplied liquid water. The gaseous flowfield includes the motor exhaust gases as well as the ambient air and vaporized water. Enforcing the conservation of mass, momentum, and energy between the two models provides the coupling. At any instant the water vaporization rate is interpreted as a water vapor or steam source in the gaseous model. Also, the momentum and energy associated with this water source as well as the drag and heat flux at the water–gas interface define the source of momentum and energy in the gaseous model. In this study the gaseous phase is modeled as an inviscid flow. However, the drag and heat exchange between the water droplets and the gaseous phase is accounted for by means of source terms in the gaseous-phase governing equations as discussed next. Also, the model omits chemical reactions; therefore, the effects of afterburning of fuel-rich exhaust on the ignition overpressure (IOP) is not accounted for.

A. Gas-Phase Model

In the absence of the viscous effects, the gaseous flowfield is governed by the nonlinear Euler system of equations. These can be written as

$$\frac{\partial \boldsymbol{U}}{\partial t} + \frac{\partial \boldsymbol{F}_m}{\partial x_m} = \boldsymbol{B} \tag{1}$$

with

$$\boldsymbol{U} = \begin{bmatrix} \rho Y_1 \\ \rho Y_2 \\ \vdots \\ \rho Y_i \\ \rho v_n \\ \rho E \end{bmatrix}, \qquad \boldsymbol{F}_m = \begin{bmatrix} \rho Y_1 v_m \\ \rho Y_2 v_m \\ \vdots \\ \rho Y_i v_m \\ \rho v_m v_n + P\delta_{mn} \\ \rho v_m (E + P/\rho) \end{bmatrix}$$

$$\boldsymbol{B} = \begin{bmatrix} \dot{m}_1''' \\ \dot{m}_2''' \\ \vdots \\ \dot{m}_i''' \\ \dot{m}_j'''(V_n)_j - D_n \\ \dot{m}_j'''(h_g)_j - \dot{q} \end{bmatrix} \tag{2}$$

where $E = \varepsilon + \frac{1}{2} v_m v_m$ and $\varepsilon = c_v T = c_p T - P/\rho$. Here, repeated index implies summation. Finally, assuming that the mixture and each of its constituents behaves as an ideal gas, the closure is formed with the equation of state for an ideal flow, $P = \rho RT$.

B. Liquid-Water Supply Model

The supplied liquid water is modeled as a collection of spherical water droplets. The water injection is then simulated with a spray model. The dynamics of each individual droplet is simulated by imposing the conservation of mass, momentum, and energy as they interact with the surrounding gaseous flow. At the prescribed injection point, a stream of water droplets is introduced with diameters equal to the exit diameter of the water-injection nozzle.[13] The rate at which these droplets are introduced is prescribed according to the desired water addition mass flow rate. Once a water droplet is introduced, its trajectory, vaporization rate, diameter, etc., will depend on its interaction with the surrounding gaseous flow. In addition, the droplet stability in terms of oscillation and distortion is tracked along its trajectory to determine the droplet breakup characteristics (i.e., position, diameter, velocity, etc., of the child droplets).

As just mentioned, the dynamics of a single droplet is simulated by imposing the conservation of mass, momentum, and energy. Figure 1 shows a schematic of a water droplet as it travels in a gaseous flowfield. Also shown are the key variables describing its dynamics. Ignoring variations in the flowfield within the droplet and assuming the droplet remains spherical, the conservation of mass can be expressed as

$$\frac{\mathrm{D}(\rho_d \Omega)}{\mathrm{D}t} = -\dot{m} \tag{3}$$

If the droplet density is constant, the preceding equation can be written in terms of the droplet diameter as

$$\frac{\mathrm{D}d}{\mathrm{D}t} + \frac{2\dot{m}}{\rho_d \pi d^2} = 0 \tag{4}$$

For momentum conservation, it is necessary that the rate of change in the momentum of the droplet be balanced by the net force acting upon the droplet; thus,

$$\frac{\mathrm{D}(\rho_d \Omega \boldsymbol{V}_d)}{\mathrm{D}t} = \boldsymbol{D} + (\rho_d \Omega)\boldsymbol{g} \tag{5}$$

Again, assuming constant density and substituting Eq. (3), the preceding equation can be rewritten as

$$\frac{\mathrm{D}\boldsymbol{V}_d}{\mathrm{D}t} - \frac{\dot{m}}{\rho_d \Omega}\boldsymbol{V}_d = \frac{\boldsymbol{D}}{\rho_d \Omega} + \boldsymbol{g} \tag{6}$$

Here the drag is calculated using an empirical correlation for a sphere in terms of its velocity relative to the gaseous flowfield velocity.

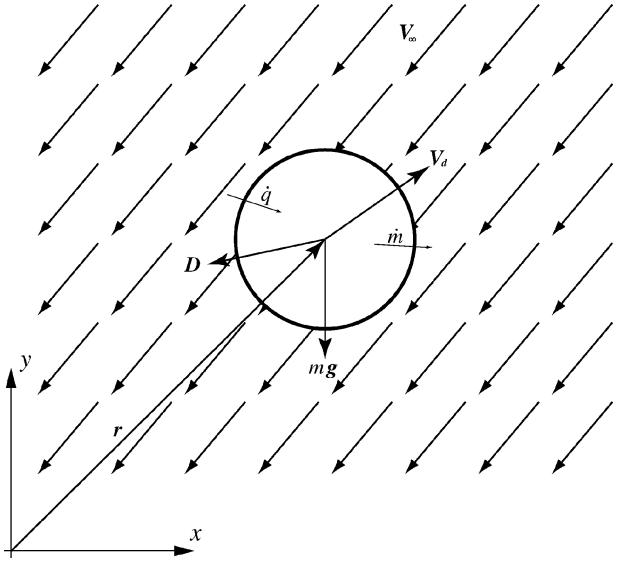

Fig. 1 Droplet dynamic variables.

Therefore, defining $\boldsymbol{V}_r$ as the velocity of the droplet relative to the gaseous flowfield, that is, $\boldsymbol{V}_r = \boldsymbol{V}_\infty - \boldsymbol{V}_d$, we have

$$|\boldsymbol{D}| = C_d \tfrac{1}{2}\rho_\infty |\boldsymbol{V}_r|^2 [(\pi/4)d^2] \tag{7}$$

The drag coefficient is calculated with the empirical correlation[14]

$$C_d = 24/Re_d + 6\Big/\left(1 + \sqrt{Re_d}\right) + 0.4 \tag{8}$$

where Re_d is the Reynolds number based on the relative velocity. The drag vector is then constructed by defining its magnitude with Eq. (7) and a unit vector parallel to $\boldsymbol{V}_r$, that is,

$$\begin{aligned} \boldsymbol{D} &= |\boldsymbol{D}|(\boldsymbol{V}_r/|\boldsymbol{V}_r|) \\ &= C_d \tfrac{1}{2}\rho_\infty [(\pi/4)d^2]|\boldsymbol{V}_r|\boldsymbol{V}_r \end{aligned} \tag{9}$$

Finally, for energy conservation we must have the rate of change in the droplet total energy balanced by the net heat absorbed and net work done by the forces acting upon the droplet; thus,

$$\frac{\mathrm{D}\left[\rho_d \Omega\left(C\,T_d + \tfrac{1}{2}\boldsymbol{V}_d \cdot \boldsymbol{V}_d + \boldsymbol{r}\cdot\boldsymbol{g}\right)\right]}{\mathrm{D}t} = (\dot{q} - \dot{m}h_{\mathrm{fg}}) + (\rho_d \Omega)\boldsymbol{g}\cdot\boldsymbol{V}_d \tag{10}$$

Substituting Eqs. (4) and (6) into Eq. (10) and simplifying, we have

$$\frac{\mathrm{D}T_d}{\mathrm{D}t} = \frac{(\dot{q} - \dot{m}h_{\mathrm{fg}})}{\rho_d \Omega C} \tag{11}$$

Implicit in Eq. (10) or (11) is a discontinuity in the temperature, heat absorbed, and vaporization rate. As the droplet travels through the gaseous flowfield, it absorbs heat, increasing its temperature up to the saturation temperature. At this point any additional heat added would result in the vaporization of the droplet. With the droplet temperature below the saturation temperature, the vaporization rate is equal to zero. Therefore, Eq. (11) can be explicitly written as

$$\frac{\mathrm{D}T_d}{\mathrm{D}t} = \begin{cases} \dfrac{\dot{q}}{\rho_d \Omega C}, & T_d < T_{\mathrm{sat}};\ \dot{m} = 0 \\ 0, & T_d = T_{\mathrm{sat}};\ \dot{m} = \dfrac{\dot{q}}{h_{\mathrm{fg}}} \end{cases} \tag{12}$$

Here the heat absorbed $\dot{q}$ is calculated using an empirical relation for the heat-transfer coefficient h for flow passing over a sphere.[15] The expression for the heat absorbed is

$$\dot{q} = \pi d^2 h(T_{\mathrm{aw}} - T_d), \qquad h = (k_\infty/d)Nu_d \tag{13}$$

The Nusselt number Nu_d is given in terms of the Reynolds number Re_d and the Prandtl number Pr by the empirical equation[16]

$$Nu_d = 2 + 0.6Re_d^{\frac{1}{2}} Pr^{\frac{1}{3}} \tag{14}$$

where the Prandtl number is evaluated using properties from the gaseous flowfield.

To simulate the droplet breakup phenomenon, the Taylor analogy breakup (TAB) model by O'Rourke and Amsden is used.[13] In their breakup model the stability of the droplet is described by the ordinary differential equation

$$\ddot{y} + \left(2\frac{\dot{d}}{d} + \frac{20\mu}{\rho_d d^2}\right)\dot{y} + \left(\frac{\ddot{d}}{d} + \frac{\dot{d}}{d}\frac{20\mu}{\rho_d d^2} + \frac{64\sigma}{\rho_d d^3}\right)y = \frac{8}{3}\frac{\rho_\infty}{\rho_d}\left(\frac{|\boldsymbol{V}_r|}{d}\right)^2 \tag{15}$$

where breakup occurs if and only if $y > 1$. For constant $|\boldsymbol{V}_r|$ and d, the solution to Eq. (15) is

$$\begin{aligned} y(t) = We/12 &+ e^{-t/t_d}\{(y_0 - We/12)\cos\omega t \\ &+ (1/\omega)[\dot{y}_0 + (1/t_d)(y_0 - We/12)]\sin\omega t\} \end{aligned} \tag{16}$$

where

$$t_d = \rho_d d^2 \big/ 10\mu, \qquad \omega^2 = 64\sigma \big/ \rho_d d^3 - 1\big/t_d^2 \tag{17}$$

The TAB model also predicts the velocity of the product droplets. This velocity is normal to the path of the parent droplet. Its magnitude is given by

$$|\boldsymbol{V}_{\text{bu}}| = (d/4)\dot{y} \tag{18}$$

The diameter of the child droplets is estimated by an equation derived by equating the oscillation energy of the parent droplet before breakup to the combined energies of the resulting droplets after breakup.[13] This procedure results in

$$d/r_{32} = 14/3 + (\rho d^3/32\sigma)\dot{y}^2 \tag{19}$$

III. Method of Solution

The numerical methodology employed to solve Eq. (1) can be described as a combination of a temporal discretization scheme, a spatial discretization scheme, and a discontinuity-capturing scheme. In the time discretization scheme the value of $\boldsymbol{U}$ is sought given its value at a previous time by means of a Taylor-series expansion. The spatial discretization is done using the Galerkin finite element method in which the integrated weighted residual is minimized. To resolve discontinuities in the flowfield, a convective flux correction term is devised following the work of Davis.[17] This scheme is then combined with a Lagrangian approach to analyze the motion of the water droplets.

A. Temporal Discretization Scheme

The Taylor-series expansion of $\boldsymbol{U}$ can either be expressed explicitly as

$$\overset{\text{exp}}{\Delta\boldsymbol{U}}{}^{l+1} = \Delta t \frac{\partial \boldsymbol{U}}{\partial t}\bigg|^{l} + \frac{\Delta t^2}{2}\frac{\partial^2 \boldsymbol{U}}{\partial t^2}\bigg|^{l} + \sum_{m=3}^{\infty}\frac{\Delta t^m}{m!}\frac{\partial^m \boldsymbol{U}}{\partial t^m}\bigg|^{l} \tag{20}$$

or implicitly as

$$\overset{\text{imp}}{\Delta\boldsymbol{U}}{}^{l+1} = \Delta t \frac{\partial \boldsymbol{U}}{\partial t}\bigg|^{l+1} - \frac{\Delta t^2}{2}\frac{\partial^2 \boldsymbol{U}}{\partial t^2}\bigg|^{l+1} + \sum_{m=3}^{\infty}(-1)^m\frac{\Delta t^m}{m!}\frac{\partial^m \boldsymbol{U}}{\partial t^m}\bigg|^{l+1} \tag{21}$$

where the superscripts $l+1$ and l indicate that the quantity is evaluated at $t+\Delta t$ or at t, respectively. A linear combination of Eqs. (20) and (21) results in an expression that preserves both the explicit and implicit characteristics

$$\begin{aligned}\Delta\boldsymbol{U}^{l+1} &= (1-s)\overset{\text{exp}}{\Delta\boldsymbol{U}}{}^{l+1} + s\overset{\text{imp}}{\Delta\boldsymbol{U}}{}^{l+1}\\ &= \Delta t\left[\frac{\partial \boldsymbol{U}}{\partial t}\bigg|^{l} + s\left(\frac{\partial \boldsymbol{U}}{\partial t}\bigg|^{l+1} - \frac{\partial \boldsymbol{U}}{\partial t}\bigg|^{l}\right)\right] + \frac{\Delta t^2}{2}\\ &\quad\times\left[\frac{\partial^2 \boldsymbol{U}}{\partial t^2}\bigg|^{l} + s\left(-\frac{\partial^2 \boldsymbol{U}}{\partial t^2}\bigg|^{l+1} - \frac{\partial^2 \boldsymbol{U}}{\partial t^2}\bigg|^{l}\right)\right] + \mathcal{O}(\Delta t^3)\end{aligned} \tag{22}$$

where $0 \le s \le 1$. Here, following the work of Schunk et al.,[18] the level of flexibility can be taken one step further by decoupling the level of implicitness of the first-order term from that of the second-order term. This is achieved by splitting the parameter s into s_1 and s_2, where s_1 is associated with the first-order term and s_2 with the second-order term. It can be demonstrated for $0 \le s_1, s_2 \le 1$ that Eq. (2) can be rewritten as[19]

$$\begin{aligned}\Delta\boldsymbol{U}^{l+1} &= \Delta t\left(\frac{\partial \boldsymbol{U}}{\partial t}\bigg|^{l} + s_1\frac{\partial \Delta\boldsymbol{U}}{\partial t}\bigg|^{l+1}\right)\\ &\quad + \frac{\Delta t^2}{2}\left[(1-2s_1)\frac{\partial^2 \boldsymbol{U}}{\partial t^2}\bigg|^{l} + s_2\frac{\partial^2 \Delta\boldsymbol{U}}{\partial t^2}\bigg|^{l+1}\right] + \mathcal{O}(\Delta t^3)\end{aligned} \tag{23}$$

Substituting Eq. (1) into Eq. (23) and rearranging it results in

$$\boldsymbol{R} = \Delta\boldsymbol{U}^{l+1} + \frac{\partial \overline{\Delta\boldsymbol{F}}_i^{\,l+1}}{\partial x_i} + \frac{\partial \bar{\boldsymbol{F}}_i^{l}}{\partial x_i} - \Delta t(\boldsymbol{B}^{l} + s_1\Delta\boldsymbol{B}^{l+1}) \tag{24}$$

where

$$\overline{\Delta\boldsymbol{F}}_i^{\,l+1} = s_1\Delta t\Delta\boldsymbol{F}_i^{l+1} - s_2\frac{\Delta t^2}{2}\boldsymbol{a}_i^{l}\left(\frac{\partial \Delta\boldsymbol{F}_j^{l+1}}{\partial x_j} - \Delta\boldsymbol{B}^{l+1}\right) \tag{25}$$

$$\bar{\boldsymbol{F}}_i^{l} = \Delta t\boldsymbol{F}_i^{l} - (1-2s_1)\frac{\Delta t^2}{2}\boldsymbol{a}_i^{l}\left(\frac{\partial \boldsymbol{F}_j^{l}}{\partial x_j} - \boldsymbol{B}^{l}\right) \tag{26}$$

and $\boldsymbol{a}_i^l$ is the convective Jacobian defined as $\boldsymbol{a}_i^l \equiv (\partial \boldsymbol{F}_i/\partial \boldsymbol{U})|^l$. The relation between $\Delta\boldsymbol{U}^{l+1}$ and $\Delta\boldsymbol{F}_j^{l+1}$ is given by the Taylor-series expansion of $\boldsymbol{F} = \boldsymbol{F}(\boldsymbol{U})$ around $\boldsymbol{U}^l$ as

$$\begin{aligned}\Delta\boldsymbol{F}_i^{l+1} &= \frac{\partial \boldsymbol{F}_i}{\partial \boldsymbol{U}}\bigg|^{l}\Delta\boldsymbol{U}^{l+1} + \mathcal{O}[(\Delta\boldsymbol{U}^{l+1})^2]\\ &= \boldsymbol{a}_i^{l}\Delta\boldsymbol{U}^{l+1} + \mathcal{O}[(\Delta\boldsymbol{U}^{l+1})^2]\end{aligned} \tag{27}$$

B. Spatial Discretization Scheme

The domain is discretized in a number of finite elements formed by nodes at the vertices. Within the elements, high-order polynomials are used to interpolate the values of $\boldsymbol{U}$ from the nodes. These polynomials are usually referred to as shape functions and are denoted by $\boldsymbol{\Phi}_\alpha$, where α is the global node number. Thus, the value of $\boldsymbol{U}$ is interpolated at any point within the domain as $\boldsymbol{U}(\boldsymbol{x}) = \boldsymbol{\Phi}_\alpha(\boldsymbol{x})\boldsymbol{U}_\alpha$, where $\boldsymbol{U}_\alpha$ is the discrete nodal value of $\boldsymbol{U}$ at the node α. In the discretization scheme, a value of $\boldsymbol{U}_\alpha$ is sought such that the weighted average residual of $\boldsymbol{R}$ [Eq. (24)] integrated over the entire domain be equal to zero. For the Galerkin method the weighting function is set equal to $\boldsymbol{\Phi}_\alpha$; therefore,

$$(\boldsymbol{\Phi}_\alpha, \boldsymbol{R}) = \int_\Omega \boldsymbol{\Phi}_\alpha \boldsymbol{R}\,\mathrm{d}\Omega = 0 \tag{28}$$

where Ω represents the entire domain. Substituting Eq. (24) into Eq. (28) and integrating by parts results in

$$\begin{aligned}\int_\Omega \boldsymbol{\Phi}_\alpha\Delta\boldsymbol{U}^{l+1}\,\mathrm{d}\Omega &= \int_\Omega \overline{\Delta\boldsymbol{F}}_m^{\,l+1}\frac{\partial \boldsymbol{\Phi}_\alpha}{\partial x_m}\,\mathrm{d}\Omega\\ &\quad - \int_\Gamma \boldsymbol{\Phi}_\alpha\overline{\Delta\boldsymbol{F}}_m^{\,l+1}\,\mathrm{d}\Gamma_m + \int_\Omega \boldsymbol{\Phi}_\alpha\Delta\boldsymbol{B}^{l+1}\,\mathrm{d}\Omega\\ &\quad + \int_\Omega \bar{\boldsymbol{F}}_m^{l}\frac{\partial \boldsymbol{\Phi}_\alpha}{\partial x_m}\,\mathrm{d}\Omega - \int_\Gamma \boldsymbol{\Phi}_\alpha\overline{\boldsymbol{F}}_m^{l}\,\mathrm{d}\Gamma_m + \int_\Omega \boldsymbol{\Phi}_\alpha\boldsymbol{B}^{l}\,\mathrm{d}\Omega\end{aligned} \tag{29}$$

C. Discontinuity Capturing Scheme

Without modification, the flux approximation of Eq. (25) or (26) satisfies neither the entropy nor the monotone conditions. Therefore, this flux approximation has to be corrected to avoid the introduction of expansion shocks and dispersion error. To avoid the generation of dispersion error, a correction term, which enforces the monotone condition, is formulated. This correction term is obtained by reformulating Eq. (26) in terms of split flux vectors. Limiter functions are then introduced in order to limit the high-order terms. The resulting flux vector approximation is

$$\begin{aligned}\bar{\boldsymbol{F}}_m^{l} &= \Delta t\boldsymbol{F}_m^{l} - \frac{\Delta t^2}{2}(1-2s_1)\boldsymbol{a}_m^{l}\left(\frac{\partial \boldsymbol{F}_n^{l}}{\partial x_n} - \boldsymbol{B}^{l}\right) + \left(\Psi_{(m)}^{+} + \Psi_{(m)}^{-} - 1\right)\\ &\quad\times\left[\frac{\Delta t h_{(m)}}{2}\frac{\partial |\boldsymbol{F}_m^{l}|}{\partial x_{(m)}} - \frac{\Delta t^2}{2}(1-2s_1)\left|\boldsymbol{a}_m^{l}\right|\frac{\partial |\boldsymbol{F}_n^{l}|}{\partial x_n}\right]\end{aligned} \tag{30}$$

where $|\boldsymbol{F}_m^{l}| = \boldsymbol{F}_m^{+l} - \boldsymbol{F}_m^{-l}$. The third term on the right-hand side is the flux correction term. As proposed by Davis,[17] this term can be approximated using the one-wave Riemann solver as

$$\begin{aligned}\bar{\boldsymbol{F}}_m^{l} &= \Delta t\boldsymbol{F}_m^{l} - \frac{\Delta t^2}{2}(1-2s_1)\boldsymbol{a}_m^{l}\left(\frac{\partial \boldsymbol{F}_n^{l}}{\partial x_n} - \boldsymbol{B}^{l}\right) + \left(\Psi_{(m)}^{+} + \Psi_{(m)}^{-} - 1\right)\\ &\quad\times\left[\frac{\Delta t h_{(m)}}{2}\left|\overset{\max}{\lambda_m}\right|\frac{\partial \boldsymbol{U}^{l}}{\partial x_{(m)}} - \frac{\Delta t^2}{2}(1-2s_1)\left|\overset{\max}{\lambda_m}\right|\left|\overset{\max}{\lambda_n}\right|\frac{\partial \boldsymbol{U}^{l}}{\partial x_n}\right]\end{aligned} \tag{31}$$

It has been demonstrated that this formulation prevents the generation of expansion shocks.[17] This could be accredited to the use of the absolute maximum value of the eigenvalues, which precludes the zero value at sonic points within expansion regions. The original definition of the limiter as proposed by Davis[17] is of the form

$$\Psi_{(m)}\left(r^{+}_{(m)}, r^{-}_{(m)}\right) = \Psi^{+}_{(m)} + \Psi^{-}_{(m)}$$
$$= \max\left[0, \min\left(2r^{+}_{(m)}, r^{-}_{(m)}, 1\right), \min\left(2r^{-}_{(m)}, r^{+}_{(m)}, 1\right)\right] \tag{32}$$

with

$$r^{+}_{(m)} = \frac{\boldsymbol{U}_{,\,(m)} \cdot \left(\boldsymbol{U}_{,\,(m)} - h_{(m)}\boldsymbol{U}_{,\,(m)(m)}\right)}{\left\|\boldsymbol{U}_{,\,(m)}\right\|^2}$$

$$r^{-}_{(m)} = \frac{\boldsymbol{U}_{,\,(m)} \cdot \left(\boldsymbol{U}_{,\,(m)} + h_{(m)}\boldsymbol{U}_{,\,(m)(m)}\right)}{\left\|\boldsymbol{U}_{,\,(m)}\right\|^2} \tag{33}$$

where $\boldsymbol{U}_{,m} = \partial \boldsymbol{U}/\partial x_m$. Here, the parentheses in the subscript indicate that the summation rule does not apply.

D. Water Spray Solution

The system of the coupled ordinary differential equations given by Eqs. (4), (6), and (12) is integrated using the fourth-order Runge–Kutta method.[20] The implementation of the droplets breakup model follows the work of O'Rourke and Amsden.[13] The diameter and velocity of the child droplets are then calculated using Eqs. (18) and (19). The value calculated from Eq. (18) is the velocity magnitude of the child droplet relative to the parent droplet. The direction of this relative velocity is normal to the path of the parent droplet. Therefore, the resulting child droplet velocity is calculated as

$$\overset{\text{child}}{\boldsymbol{V}_d} = \overset{\text{parent}}{\boldsymbol{V}_d} + |\boldsymbol{V}_{\text{bu}}|\boldsymbol{n} \tag{34}$$

where $\boldsymbol{n}$ is a unit vector normal to the path of the parent droplet. For a two-dimensional calculation, $\boldsymbol{n}$ can be calculated as

$$\boldsymbol{n} = \boldsymbol{u} \times \left(\overset{\text{parent}}{\boldsymbol{V}_d} \Big/ \overset{\text{parent}}{|\boldsymbol{V}_d|}\right) \tag{35}$$

where $\boldsymbol{u}$ is the unit vector normal to the plane.

IV. Results and Discussion

The results presented focus on the ignition overpressure generated by a representative launch-vehicle/launchpad configuration. The launch-vehicle dimensions, motor size, and motor startup transient characteristics are based on the first stage of the Minuteman missile.[4] The launchpad consists of a simple rigid plate. This configuration, although idealized, could be described as representative of current configurations of interest such as the Delta rocket and the solid rocket booster of the space transportation system (STS).[21]

This investigation proceeds through a series of numerical solutions. First, the ignition overpressure generated by the selected representative configuration is studied without any water addition. These results are used as the baseline model in this investigation. Then, results of a preliminary study are shown based on a simplified water addition model. In this model the water is introduced into the rocket plume as an exchange of sensible heat from the gases. That is, the energy associated with the added water is subtracted from the gases. This substantially limits the amount of water that can be added to the plume. Nevertheless, this preliminary study provided some interesting insights into the behavior of the rocket plume with water addition. Following this preliminary study, results based on a higher-fidelity model of a water addition source are presented. In this model, the restriction on the rate of water addition is removed allowing the simulation of representative values of water addition rates.

A. Baseline Configuration

Figure 2 shows the launchpad/vehicle configuration selected for this study. The computational domain includes the motor chamber and nozzle as well as the motor and vehicle surroundings. The entire domain, including the motor, vehicle, and its surrounding, is discretized into 50,000 nodes arranged in an unstructured mesh. The mesh is made up of triangular elements with smaller size elements near the motor as shown in Fig. 3. The higher concentration of smaller elements within the motor and near the motor nozzle exit provides the required resolution for the proper numerical prediction of the flowfield within these regions. This element size distribution was obtained through a grid-independence study.

The calculation was performed in a 10-CPU, R12000 Silicon Graphics machine. The simulation time was 0.5 s for which approximately 20 CPU hours were required. The calculation required a total of 40 MB of memory.

Flow total conditions are imposed at the chamber inlet and in the far field. At the motor chamber inlet, the chamber total conditions P_c and T_c are imposed. These total conditions vary with time according to the startup sequence. Also, the gas mixture entering the chamber represents the equilibrium mixture of the combustion products. In the far field, the total conditions are fixed at $P_0 = 1$ atm and $T_0 = 300$ K, and the gas is air. Finally, all of the solid surfaces are considered as rigid slip walls. These include the motor interior walls, the vehicle surface, and the launchpad surface.

The motor illustrated in Fig. 2 was sized according to the first stage of the Minuteman missile motor. The motor net throat diameter is 0.762 m, the nozzle net area ratio is 7.11, and the thrust level is 890 kN. As stated earlier, these values are based on the cumulative effect of the four smaller thrusters of the Minuteman clustered motor. A typical startup sequence for this motor is shown in Fig. 4 (Ref. 4).

At $t = 0$, the simulation begins and proceeds while adjusting the chamber pressure and temperature according to the distribution shown in Fig. 4. The steady-state chamber pressure $(P_c)_{ss}$ is 5.5 MPa for which the motor mass flow rate is 310 kg/s. The steady-state

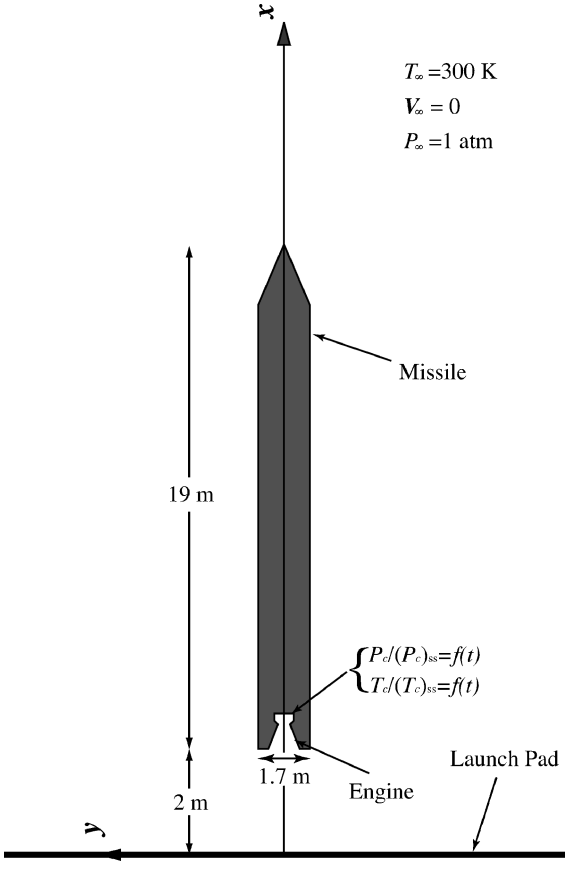

Fig. 2 Representative launchpad/vehicle configuration.

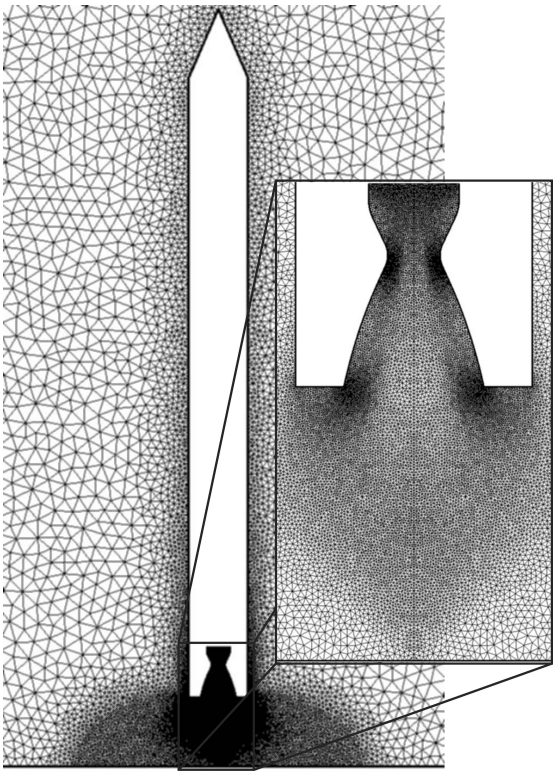

Fig. 3 Computational grid.

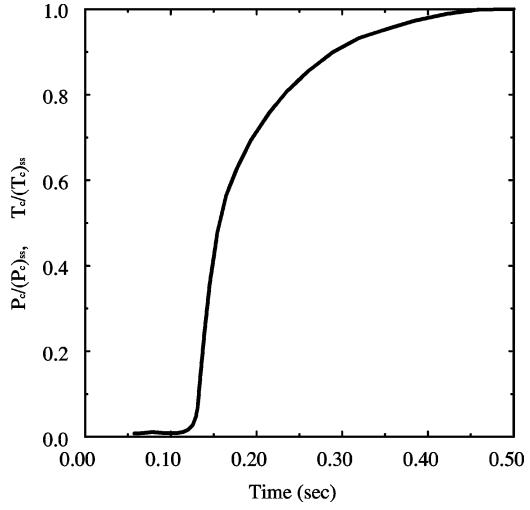

Fig. 4 Minuteman (or baseline) chamber pressure and temperature as function of time.

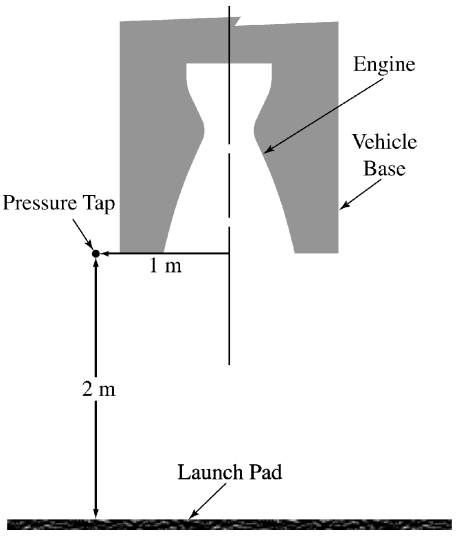

Fig. 5 Location of monitor point for predicted pressure ("tap").

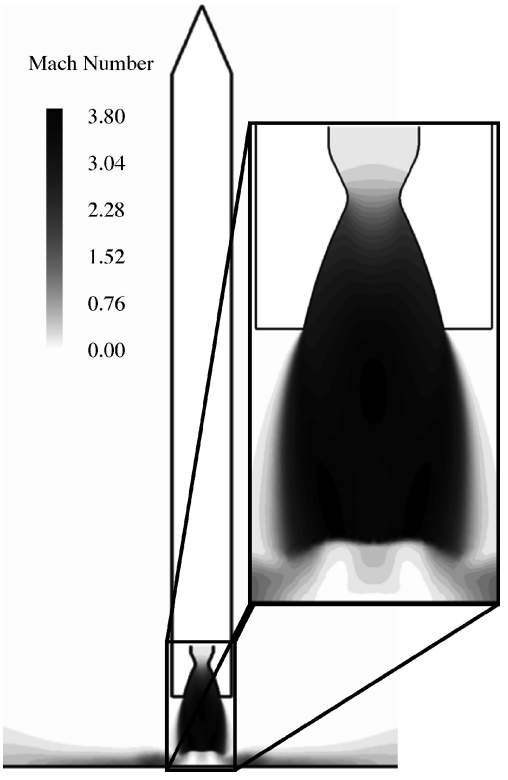

Fig. 6 Predicted Mach-number distribution (baseline configuration, $t = 0.5$ s).

chamber temperature $(T_c)_{ss}$ is 3200 K. The steady-state chamber pressure and temperature are achieved after approximately 0.5 s as shown in Fig. 4. Although the data shown in Fig. 4 are the measured chamber pressure, in this study the average normalized total chamber temperature was assumed to have the same temporal behavior. During the simulation, the pressure is monitored at a pressure tap located near the vehicle base as shown in Fig. 5.

Figures 6 and 7 show the instantaneous Mach number and streamline distributions at $t = 0.5$ s, respectively. As shown, the steady-state flowfield consists of a supersonic exhaust stream impinging on the launchpad. The surrounding air is entrained into the plume toward the vehicle base and then convected away from the motor exhaust plume. These results correspond to the baseline case where no water has been added to the motor plume. Figure 8 shows the overpressure history at a pressure tap near the vehicle base. The predicted ignition overpressure is approximately 10 kPa. The maximum ignition overpressure is reached at approximately 0.15 s, corresponding to the highest rate of chamber pressure increase as shown in Fig. 9a. Also shown in this figure is the meassured rate of chamber pressure change as a function of time for the STS solid rocket motor. As compared with the baseline configuration, the maximum rate of chamber pressure increase in the solid rocket motor is approximately half of that in the baseline configuration. According to the work of Jones,[11] the overpressure wave satisfies the proportional relation $\Delta P \propto A^* \dot{P}_c^2 / P_c$. Using this relation, the overpressure history shown in Fig. 8 is scaled and compared to the overpressure history measured at the base of the shuttle as shown in Fig. 10.

B. Preliminary Overpressure Suppression Study

In the preliminary study, five different water addition configurations were studied to determine the effect of water addition on

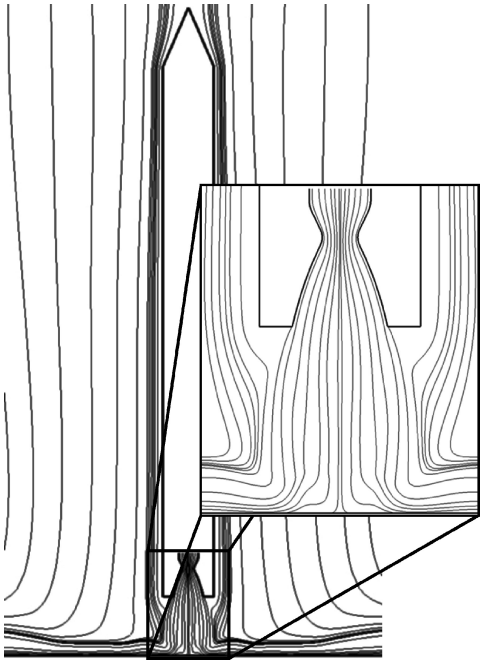

Fig. 7 Predicted streamline distribution (baseline configuration, $t = 0.5$ s).

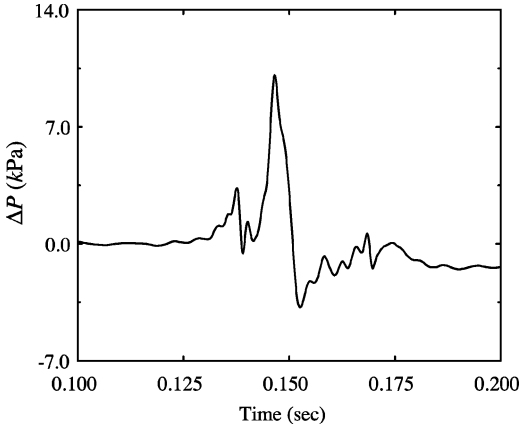

Fig. 8 Predicted overpressure history at the pressure monitor point.

the ignition overpressure. Figure 11 shows illustrations of each of the water addition configurations studied. In configuration A, water is injected with zero velocity within the plume 25.4 cm downstream of the nozzle exit plane. In configuration B, the water addition region is moved an additional 76.2 cm away from the nozzle exit plane. In configuration C, the water addition region is moved out of the plume. However, the water is injected with a nonzero velocity toward the plume. In configuration D, water is added only to the region of the plume near the launch-pad surface. In this configuration the water is also added with zero velocity. Finally, in configuration E, water is added in a relatively small region at the center of the plume. Depending on the configuration, the water-injection rate was varied from 0.002 to 0.12 gallons per minute (gpm). These are relatively small water-injection rates when compared to the STS. In the STS the water-injection rates are approximately equal to the propellants mass flow rate,[21] whereas, in this preliminary analysis, the water-injection rates are approximately 1/10th of the propellants, mass flow rate. However, in this preliminary investigation the amounts of water added correspond only to the water vaporized by the plume gas stream.

Figure 12 shows a comparison between overpressure histories for the baseline configuration and configuration A. As shown in this

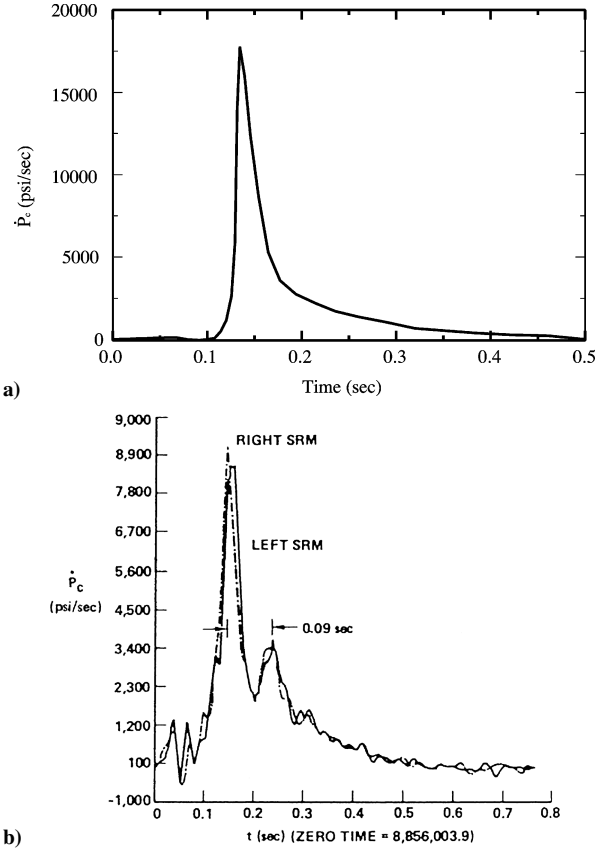

Fig. 9 Chamber pressurization rate: a) baseline configuration and b) space shuttle booster.

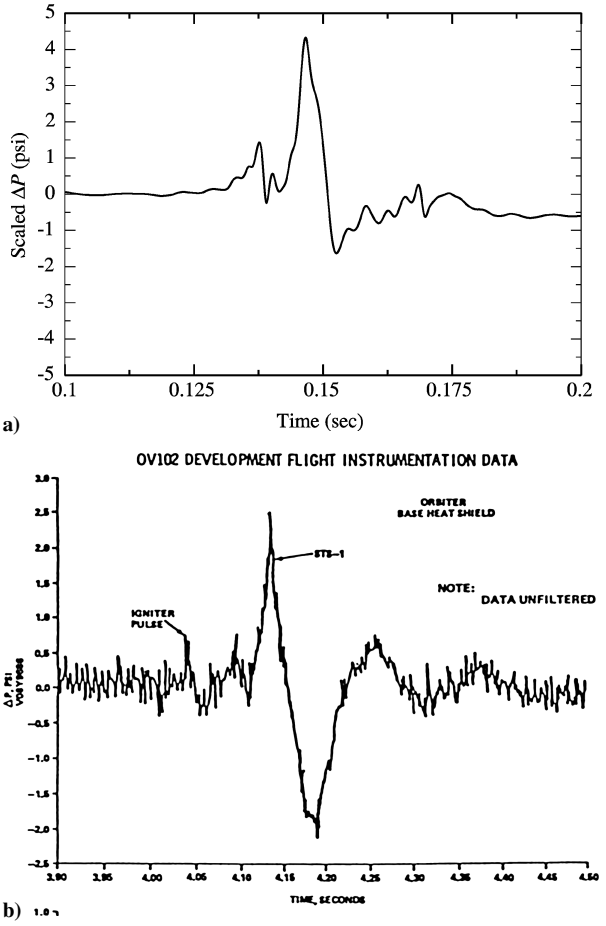

Fig. 10 Overpressure history: a) scaled pressure for the baseline configuration and b) space shuttle booster.

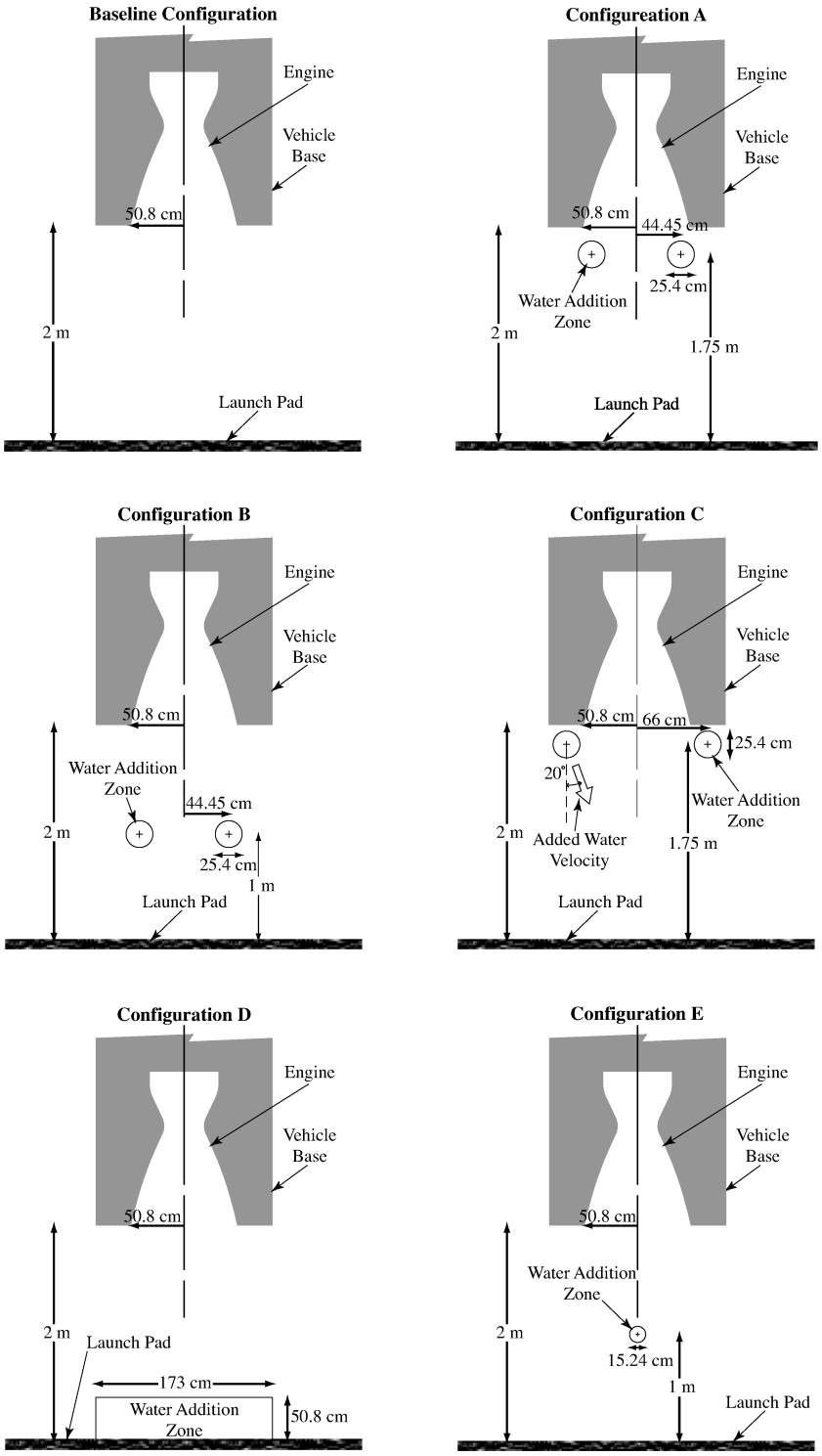

Fig. 11 Water addition configurations for the preliminary study.

figure, as the rate of water injection is increased the ignition overpressure increases. The simulation performed with configuration A shows that doubling the water-injection rate results in an increase in the ignition overpressure of approximately 30%. This is explained in terms of the amount of obstruction in the plume flow area. As the water addition rate is increased, more mass of slow moving water and combustion products accumulate near the nozzle exit plane, effectively reducing the nozzle exit area. This results in a more confined expansion of the plume causing the increase in the ignition overpressure. Similar behavior was observed with configuration C. In this configuration the water addition region has been moved out of the plume flowpath. Although the obstruction to the plume expansion is reduced, the interaction between the added water and the overpressure wave front is reduced as well, resulting in a less effective configuration as compared to configuration A.

Figure 13 shows the comparison between the overpressure histories of the baseline configuration and configurations A and B. As seen in this figure, configuration B resulted in a 10% decrease in the ignition overpressure as compared with the baseline configuration. By comparing the results for configurations A and B, it is apparent that the effect of the water injection is extremely dependent on the location of the water mass addition. It can be deduced that the

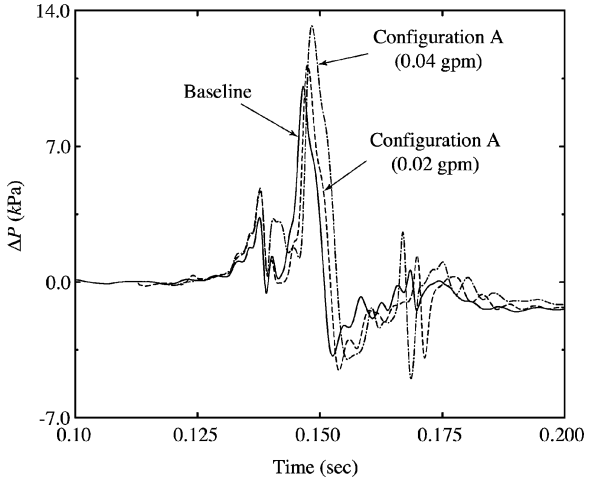

Fig. 12 Overpressure histories for the baseline and configuration A.

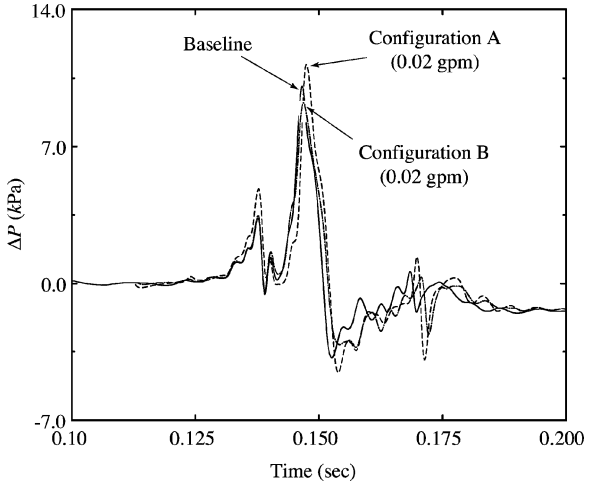

Fig. 13 Overpressure histories for the baseline and configurations A and B.

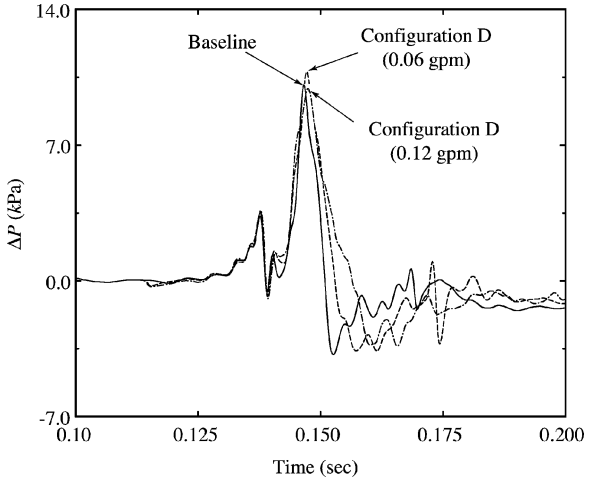

Fig. 14 Overpressure histories for the baseline and configuration D.

difference in results can be attributed to a balance between the obstruction caused by the water near the nozzle exit and the effect of removing energy from the plume by the cooling of the plume by the water.

Figure 14 shows the comparison between the pressure–time histories of the baseline configuration and configuration D at two different water-injection rates. The figure illustrates the balance between the induced "obstruction" to the plume stream and the effect of cooling

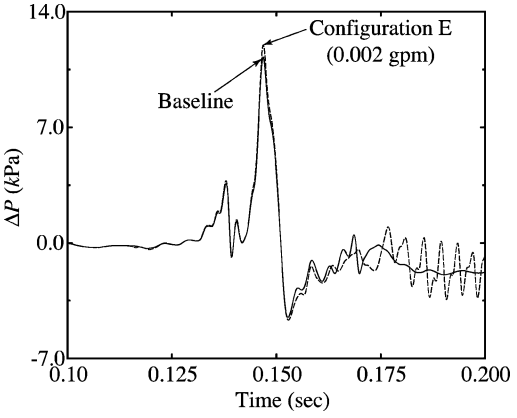

Fig. 15 Overpressure histories for the baseline and configuration E.

of the plume gases. As the rate of water addition is increased in configuration D, the ignition overpressure increases. This pattern continues until a water addition rate of approximately 0.06 gpm is achieved. Further increases in the water addition rate beyond 0.06 gpm cause a decrease in the ignition overpressure. At a water addition rate of 0.12 gpm, the ignition overpressure is reduced by approximately 3% relative to the baseline.

Figure 15 shows the comparison between the pressure–time histories of the baseline configuration and configuration E. For a given water addition rate, the highest overpressure was observed for configuration E. In this configuration, the accumulation of water at the center of the plume induces the formation of a shock closer to the nozzle exit as compared with the other configurations. Figure 16 shows the water mass fraction and pressure distributions for configuration E at $t = 0.15$ s. Another reason for the poor performance of this configuration is caused by a less effective cooling as compared to the other configurations. This is because in configuration E the water injected is concentrated in a smaller region as compared to the other configurations.

C. Detailed Overpressure Suppression Study

This study implements a higher-fidelity water addition model where the restriction on the rate of water addition has been removed. Also, unlike the previous study, the interactions between the liquid water spray and the exhaust gases are included in the model to dynamically predict the water source distribution. This allows a more realistic assessment of the effectiveness of the overpressure suppression technique by water addition. In what follows, six additional water addition configurations are evaluated and compared. Figure 17 shows one of the configurations studied. In this configuration, an array of 36 identical water nozzles is distributed uniformly around the plume circumference near the nozzle exit. The nozzles are distributed uniformly around the motor nozzle exit as shown in Fig. 17a. Each water nozzle injects a stream of water droplets toward the plume with a velocity vector perpendicular to the motor nozzle axis. In configuration F, the diameter of the water nozzles is 2.54 cm, the water volume flow rate is 5700 gpm, and the water nozzle pressure drop is 450 kPa. In configuration G, the water nozzle arrangement is moved down 1 m toward the launchpad surface while all other parameters remain fixed. For configuration H, the diameter of the water nozzles is reduced to 1.27 cm, and the water nozzle pressure drop is increased to 7.2 MPa. In configuration I the water volume flow rate is increased by a factor of 10 to 57,000 gpm while keeping the water nozzle diameter at 2.54 cm resulting in a water nozzle pressure drop of 45 MPa. In configuration J the water volume flow rate is reduced by a factor of 10 to 570 gpm. As in configuration I, the water nozzle diameter is kept at 2.54 cm, resulting in a water nozzle pressure drop of 4.5 kPa. In the last configuration, configuration I is modified into configuration K, where the diameter of the water nozzles is increased to 7.62 cm resulting in a water nozzle pressure drop of 550 kPa. Table 1 contains the summary of the configurations analyzed in the detailed study.

Table 1 Summary of the configurations in the detailed study

Configuration	Volume rate, gpm	Nozzle diameter, cm	Distance from vehicle base, cm	Water nozzle ΔP, MPa
F	5,700	2.54	5	0.45
G	5,700	2.54	100	0.45
H	5,700	1.27	5	7.2
I	57,000	2.54	5	45
J	570	2.54	5	0.0045
K	57,000	7.62	5	0.55

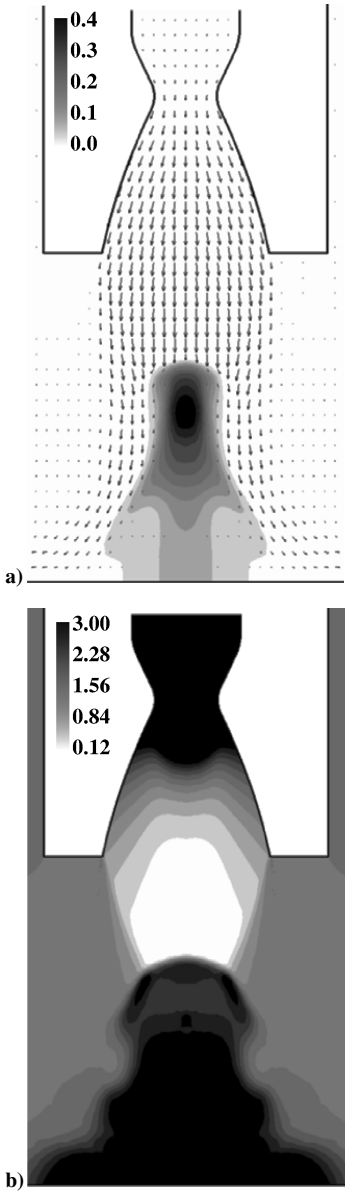

Fig. 16 Predicted flowfield at 0.15 s for configuration E: a) velocity and water concentration distributions and b) pressure distribution in atmospheres.

Figure 18 shows steam mass fraction and water droplets distribution at $t = 0.310$ s for each of the configurations studied. In this figure the droplets are sized according to the local droplet diameter. The water droplets distribution is superimposed on the steam mass concentration. For some configurations considerable water vaporization is observed, whereas for others, such as configuration I, little or no vaporization occurred. Figure 19 shows instantaneous Mach number and water droplet distributions for configuration F at a sequence of six times up to 0.31 s. At first, the stream of droplets

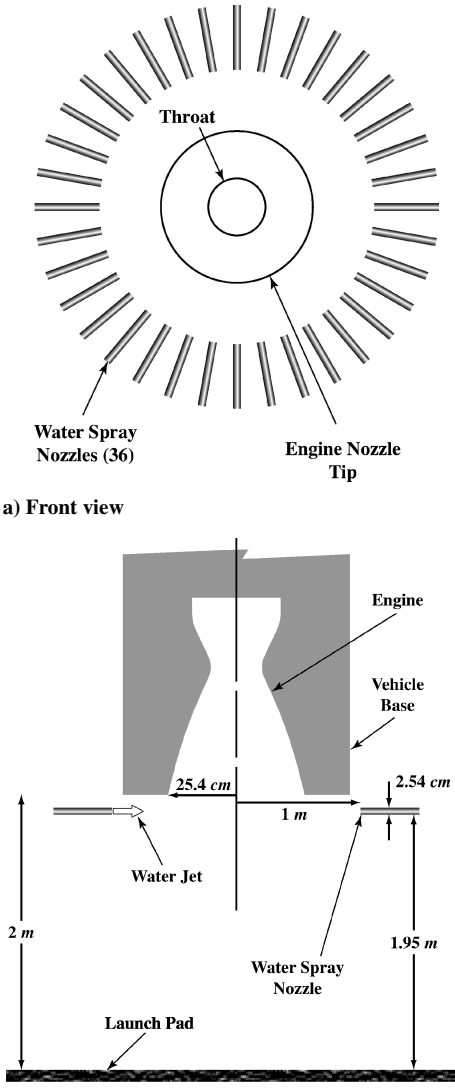

Fig. 17 Water addition configuration F for the high-fidelity study.

is essentially undisturbed until approximately the time it reaches the center of the motor nozzle. At this point, the droplet stream and the moving shock meet causing the breakup of those droplets near the motor nozzle axis. Also, the exchange in momentum between the water droplet stream and the exhaust gases induces a delay or obstruction in the expansion of the gases. In this case, this obstruction is much more severe than in the preliminary configurations because the amount of slow moving water accumulated in front of the motor nozzle is several orders of magnitude higher. Nevertheless, this higher obstruction is also associated with a higher cooling capacity. After this initial stage, the plume expands, and the droplets are dragged down toward the launchpad while they continue to break up and vaporize. After approximately 0.310 s the plume and the distribution of droplets reach steady state. Configuration F results in a considerable decrease in the ignition overpressure as compared to the baseline as shown in Fig. 20. The overpressure reduction is approximately 60%. This clearly demonstrates that the effect of the plume cooling achieved in this configuration surpasses the effect caused by the obstruction of the water accumulated in front of the motor nozzle exit. Figure 21 shows a comparison of the overpressure history obtained with configurations F and G. Although the water nozzles were moved away from the motor nozzle exit with the intent of reducing the obstruction, configuration G is a less effective configuration because it results in less reduction of the overpressure. This could be explained by the fact that in configuration G a smaller portion of the overpressure wave front interacts with

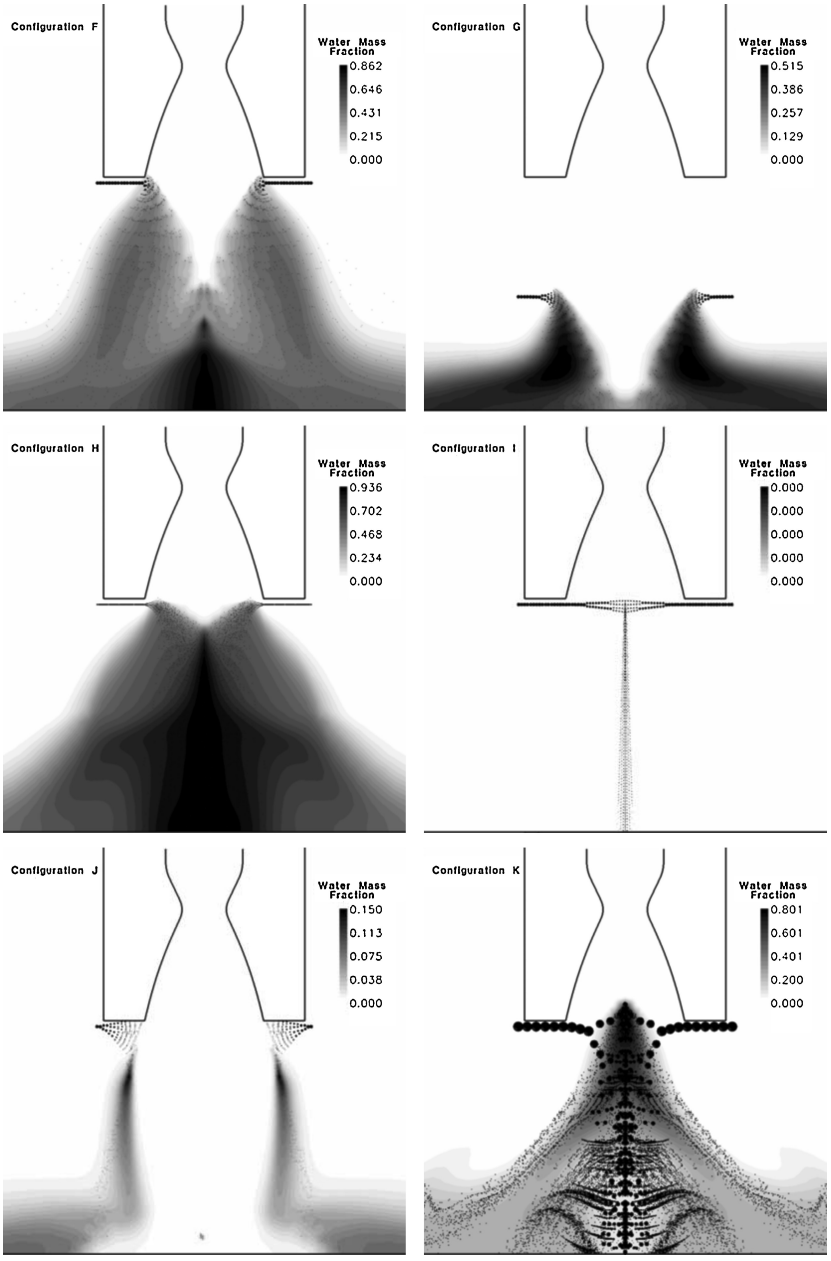

Fig. 18 Steam mass fraction and water droplet distribution at 0.31 s for configurations F–K.

the added water resulting in less cooling as compared with configuration F. In configuration H, the water nozzle diameter is reduced while the water flow rate is kept the same as compared with configuration F. This results in a higher water-injection velocity, and therefore more water is accumulated at and near the motor axis. Although a more effective cooling can be expected with smaller droplet diameter, configuration H is less effective than configuration F, as shown in Fig. 22.

An interesting comparison can be made between configurations F, I, and J. In these configurations, all of the parameters are the same except the water volume flow rate. Also, because the water nozzle diameter is the same, variations in the water volume flow rate result in variations in the water injection velocity. Figure 23 shows the comparison of the overpressure history for these configurations. This comparison leads to similar conclusions as those from Fig. 14. That is, there seems to be a balance between the amount of obstruction of the plume and the amount of cooling of the plume gases. This balance is shifted according to the rate of water addition. As the water-injection rate is increased, the cooling capacity increases, resulting in a reduction in the overpressure. Further increase of the water addition rate beyond an optimal amount would worsen the effect of obstruction and degrade the net effect of cooling.

Finally, the effect of water nozzle pressure drop is shown in Figs. 22 and 24 for water volume rates of 5700 and 57,000 gpm, respectively. These results suggest that the overpressure is more sensitive to changes in the water addition rates than changes in the water nozzle pressure drop. This is especially apparent in Fig. 24, where two orders of magnitude change in the water nozzle pressure drop resulted in a marginal change in the overpressure. It is also suggested that the effect of the water nozzle pressure drop, or the injection water velocity, on the overpressure diminishes as the water volume rates increases. At a water volume rate of 57,000 gpm, the effect of the water nozzle pressure drop is negligible as compared to the effect on the overpressure at 5700 gpm.

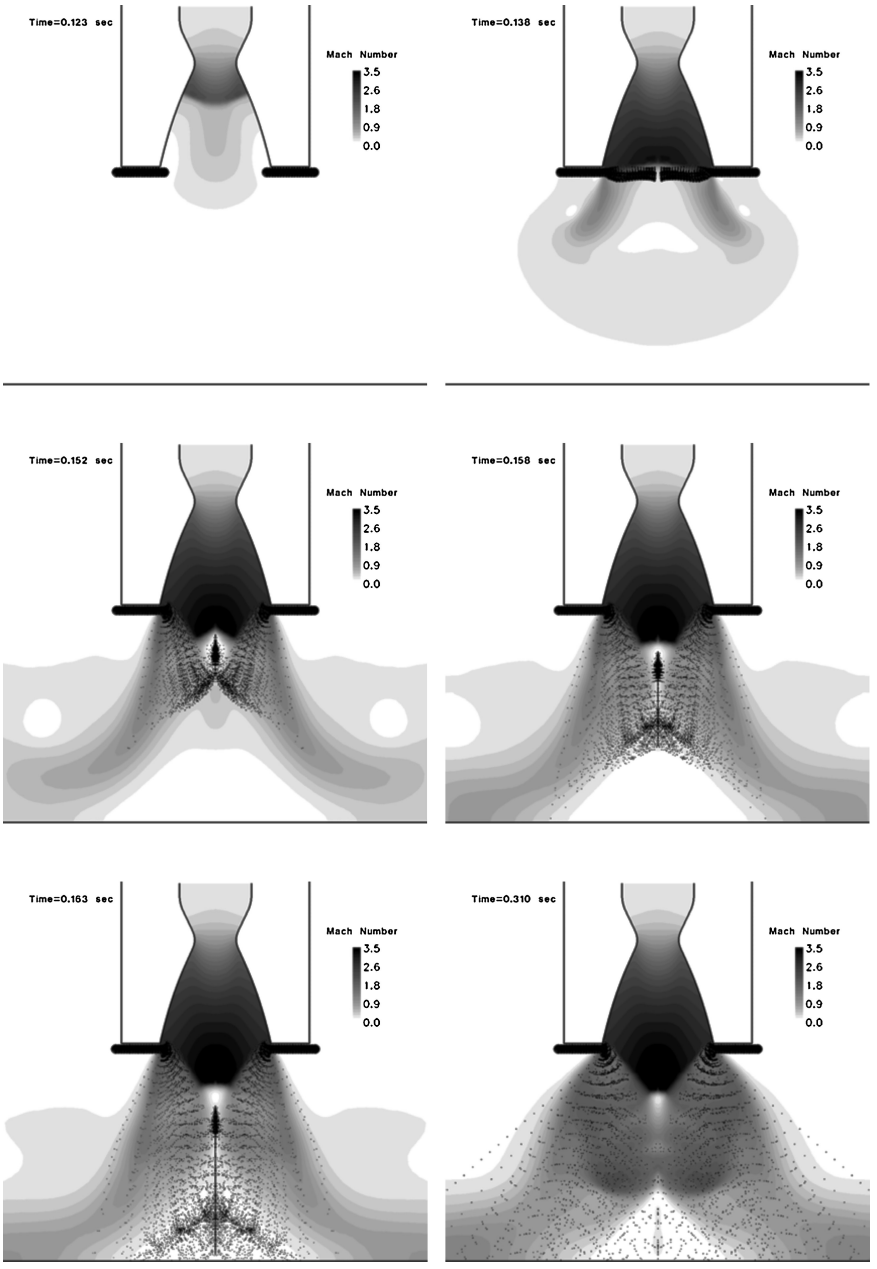

Fig. 19 Transient Mach number and water droplet distributions (configuration F).

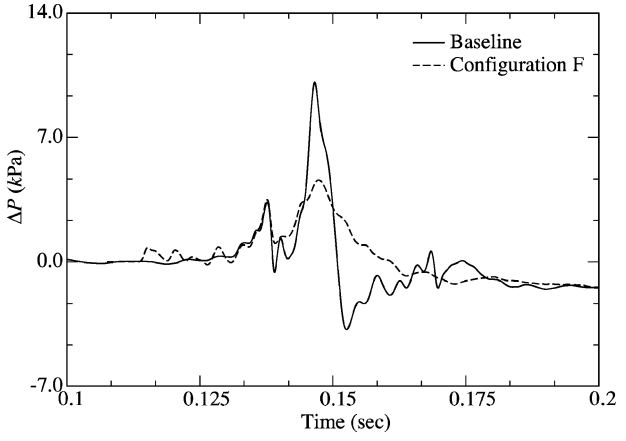

Fig. 20 Overpressure histories for the baseline and configuration F, showing a decrease in the IOP of approximately 60%.

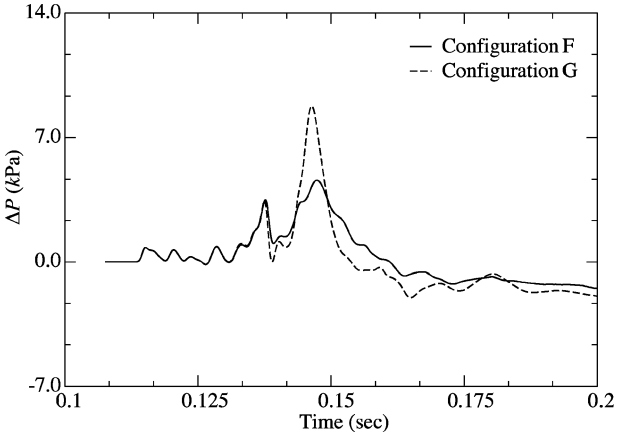

Fig. 21 Overpressure histories for configurations F and G, showing the ineffectiveness of configuration G.

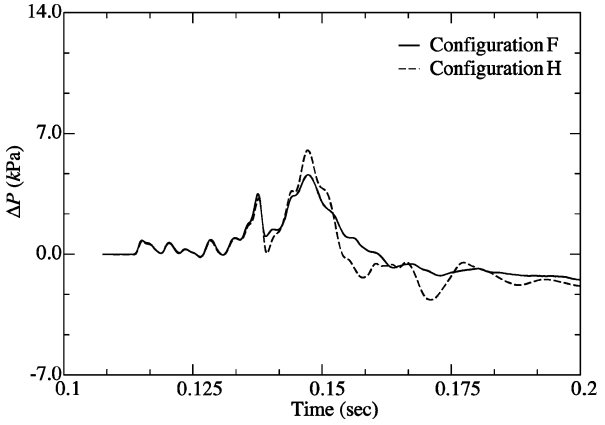

Fig. 22 Overpressure histories for configurations F and H.

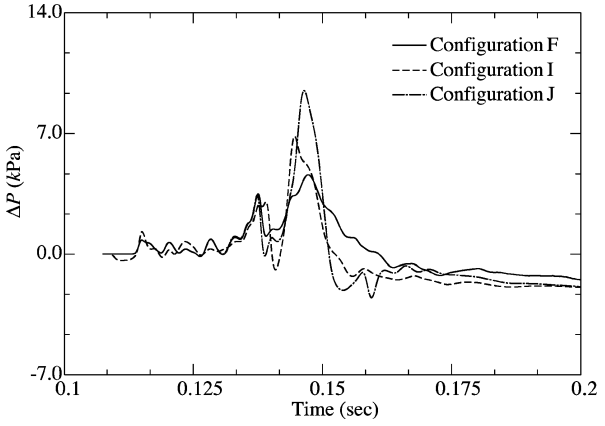

Fig. 23 Overpressure histories for configurations F, I, and J.

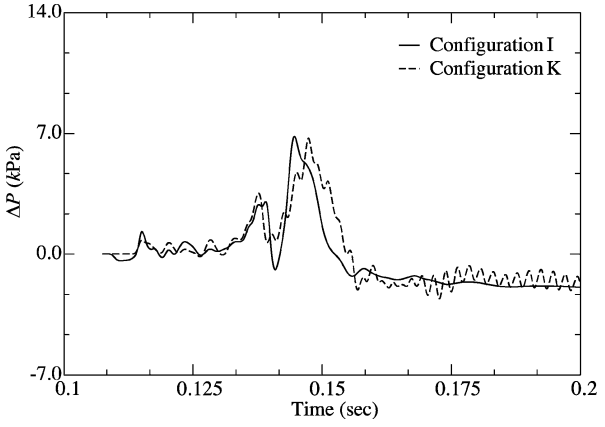

Fig. 24 Overpressure histories for configurations I and K.

V. Conclusions

The major conclusion drawn from this study is that the ignition overpressure is strongly affected by the cooling of the plume and the amount of obstruction restricting the expansion of the plume. Decreasing the enthalpy of the plume by cooling results in less available energy in the IOP to do pressure work, whereas obstructing the plume expansion turns kinetic energy into higher local pressure resulting in higher IOP. Also, the study suggests the existence of an optimal water addition rate with a weak dependence on the water nozzle pressure drop. The dependence of the IOP on the water nozzle pressure drop diminishes as the rate of water addition is increased. As the water addition rate is increased toward the optimal value, the IOP decreases. Further increase in the water addition rate beyond this optimal value does not result in a further decrease in the IOP. Therefore, the design of an efficient IOP suppression system must aim at producing the maximum amount of plume cooling while minimizing the amount of obstruction restricting the expansion of the plume. The study suggests that special attention must be given to the time interval during the startup transient at which the traveling shock wave meets the distribution of water mass accumulated near the motor nozzle axis. It is during this time interval that the overpressure suppression system can influence the magnitude of the resulting IOP. It can be speculated that the optimal amount of water addition rate is at or close to the point where the interaction between the resulting accumulated amount of water and the exiting IOP wave results in the total vaporization of the accumulated water. Any remaining liquid water in the plume, although still capable of cooling, would mostly contribute to the obstruction of the plume expansion. At this point it should be pointed out that this study does not considered the effect of afterburning, which has been proved to have a substantial influence in the IOP.[5,6] For fuel-rich motor exhaust plumes the cooling of the plume would be aggravated by the afterburning heat release resulting in higher IOP for a given water addition rate.

References

[1]Taylor, G. I., "Aerodynamics and the Mechanics of Projectiles and Explosions," *The Scientific Papers of G. I. Taylor*, Vol. 3, edited by G. K. Batchelor, Cambridge Univ. Press, Cambridge, England, U.K., 1939, pp. 221–250.

[2]Sakurai, A., "Propagation and Decay of Spherical Blast Waves," *Journal of the Physical Society of Japan*, Vol. 8, No. 5, 1953, pp. 662–700.

[3]Frendi, A., "Flammability Limits of Premixed Gases at Zero Gravity," Ph.D. Dissertation, Div. of Engineering, Brown Univ., Providence, RI, May 1990.

[4]Broadwell, J. E., and Tsu, C. N., "Transient Pressure Caused by Rocket Start and Shutdown in Ducted Launchers," *Journal of Spacecraft and Rockets*, Vol. 4, No. 10, 1967, pp. 1323–1328.

[5]Salita, M., and Glatt, L., "Modeling of Ignition Overpressure in Minuteman Silos," AIAA Paper 97-2720, July 1997.

[6]Salita, M., "Evaluation of CFD Code CFD-ACE for Rocket Applications," AIAA Paper 2000-3186, July 2000.

[7]Walsh, E. J., and Hart, P. M., "Flight Measured Lift-Off Ignition Overpressure—A Correlation with Subscale Model Tests," AIAA Paper 81-2458, 1983.

[8]Dougherty, N. S., Nesman, T. E., and Guest, S. H., "6.4% Scale Model Test Program at NASA/MSFC That Led to Overpressure Reduction of the SSV," 13th Plume Technology Conf., NASA Johnson Space Center, Houston, TX, April 1982.

[9]Shapiro, A. H., and Hawthorne, W. R., "The Mechanics and Thermodynamics of Steady One-Dimensional Gas Flow," *Journal of Applied Mechanics*, Vol. 14, No. 4, 1947, pp. A317–A336.

[10]Woo, J., Jones, J. H., and Guest, S. H., "A Study of the Effects of Water Addition on Supersonic Gas Streams," 13th Plume Technology Conf., NASA Johnson Space Center, Houston, TX, April 1982.

[11]Jones, J. H., "Scaling of Ignition Startup Pressure Transients in Rocket Systems as Applied to the Space Shuttle Over-Pressure Phenomenon," 13th Plume Technology Conf., NASA Johnson Space Center, Houston, TX, April 1982.

[12]Lai, S., and Laspesa, F. S., "Ignition Over-Pressure Measured on STS Lift-Off and Correlation with Subscale Model Tests," 13th Plume Technology Conf., NASA Johnson Space Center, Houston, TX, April 1982.

[13]O'Rourke, P. J., and Amsden, A. A., "The Tab Method for Numerical Calculation of Spray Droplet Breakup," Society of Automotive Engineers, Paper 872089, Nov. 1987.

[14]White, F. M., *Viscous Fluid Flow*, McGraw–Hill, New York, 1974, pp. 206–227.

[15]Shapiro, A. H., *The Dynamics and Thermodynamics of Compressible Fluid Flow*, Vol. 1, Wiley, New York, 1953, pp. 212, 213.

[16]Ranz, W. E., and Marshall, W. R., "Evaporation from Drops," *Chemical Engineering Progress*, Vol. 48, No. 3, 1952, pp. 141–146, 173–180.

[17]Davis, S. F., "A Simplified TVD Finite Difference Scheme via Artificial Viscosity," *SIAM Journal on Scientific and Statistical Computing*, Vol. 8, No. 1, 1987, pp. 1–18.

[18]Schunk, G., Canabal, F., Heard, G., and Chung, T. J., "Unified CFD Methods via Flowfield-Dependent Variation Theory," AIAA Paper 99-3715, June 1999.

[19]Canabal, F., "Suppression of the Ignition Overpressure Generated by Launch Vehicles," Ph.D. Dissertation, Dept. of Mechanical and Aerospace Engineering, Univ. of Alabama, Huntsville, AL, March 2004.

[20]Chapra, S. C., and Canale, R. P., *Numerical Methods for Engineers with Personal Computer Applications*, 4th ed., McGraw–Hill, New York, 2002, pp. 701–711.

[21]Kern, D., "Dynamic and Environmental Criteria," *NASA Handbook*, NASA-HDBK-7005, Jet Propulsion Lab., Pasadena, CA, 2001.

T. Lin
Associate Editor